Astronomy & Astrophysics

A solar burst with a spectral component observed only above 100 GHz during an M class flare

G. Cristiani[1], C. G. Giménez de Castro[2], C. H. Mandrini[1], M. E. Machado[3], I. de Benedetto e Silva[2], P. Kaufmann[2,4], and M. G. Rovira[1]

[1] Instituto de Astronomía y Física del Espacio, CONICET-UBA, CC 67, Suc. 28, 1428 Buenos Aires, Argentina
e-mail: gcristiani@iafe.uba.ar
[2] Centro de Rádio Astronomia e Astrofísica Mackenzie, Escola de Engenharia, R. da Consolação 896, 01302-907 São Paulo, SP, Brazil
[3] Comisión Nacional de Actividades Espaciales, Av. Paseo Colón 751, 1063 Buenos Aires, Argentina
[4] Centro de Componentes Semicondutores, UNICAMP, Campinas, Brazil

ABSTRACT

Context. Since the installation of submillimeter solar radio telescopes, a new spectral burst component was discovered at frequencies above 100 GHz, creating the *THz burst* category. In all the reported cases, the events were X-class flares and the THz component was increasing.
Aims. We report for the first time an M class flare that shows a different submillimeter radio spectral component from the microwave classical burst. Two successive bursts of 2 min duration and separated by 2 min occurred in active region NOAA 10226, starting around 13:15 UT and having an M 6.8 maximum intensity in soft X-rays.
Methods. Submillimeter flux density measured by the Solar Submillimeter Telescope (SST) is used, in addition to microwave total Sun patrol telescope observations. Images with Hα filters, from the Hα Solar Telescope for Argentina (HASTA), and extreme UV observations, from the Extreme-ultraviolet Imaging Telescope (EIT) aboard the Solar and Heliospheric Observatory (SoHO), are used to characterize the flaring region. An extensive analysis of the magnetic topology evolution is derived from the Michelson Doppler Imager (SoHO, MDI) magnetograms and used to constrain the solution space of the possible emission mechanisms.
Results. The submillimeter component is only observed at 212 GHz. We have upper limits for the emission at 89.4 and 405 GHz, which are less than the observed flux density at 212 GHz. The analysis of the magnetic topology reveals a very compact and complex system of arches that reconnects at low heights, while from the soft X-ray observations we deduce that the flaring area is dense ($n \sim 10^{12}$ cm^{-3}). The reconnected arches are anchored in regions with magnetic field intensity differing by an order of magnitude. Accordingly, we conclude that the microwave emission comes from mildly relativistic electrons spiraling down along the reconnected loops. A very small portion of the accelerated electrons can reach the footpoint with the stronger magnetic field (2000 G) and produce synchrotron emission, which is observed at submillimeter frequencies.
Conclusions. The finding of a submillimeter burst component in a medium-size flare indicates that the phenomenon is more universal than shown until now. The multiwavelength analysis reveals that neither positron synchrotron nor free-free emission could produce the submillimeter component, which is explained here by synchrotron of accelerated electrons in a rather complex and compact magnetic configuration.

Key words. Sun: flares – Sun: radio radiation

1. Introduction

The first *THz burst* ever reported is the 2003 November 4 *Halloween* flare (Kaufmann et al. 2004) observed with the Solar Submillimeter Telescope (SST). During the impulsive phase, a spectral component above 200 GHz was observed, along with the classical microwave one. Its particular characteristic is that the flux at 405 GHz is larger than at 212 GHz (optically thick emission), inverting the spectral gradient. The time profiles of the submillimeter emission coincide with the evolution at lower frequencies, though better correlated with γ and hard X-ray characteristics, indicating that very high energetic charged particles are at the origin of the submillimeter radiation. After this first THz burst, Lüthi et al. (2004b) reported the observation of a THz flare with the KOSMA 3 m telescope and a focal array at 210, 230, and 345 GHz. The increasing submillimeter spectrum was observed during the gradual phase of the burst (the system saturated during the impulsive phase). The source size could be estimated to be around 60″. Recently, two new THz events were observed: the *Halloween* 2003 November 2 (da Silva et al. 2007) and the 2006 December 6 (Kaufmann et al. 2007) flares.

All these events are of X class type and show an increasing flux density above 200 GHz. The origin of the submillimeter radiation is still controversial. It was suggested (da Silva et al. 2007) that a population of accelerated electrons in the presence of very intense magnetic fields (∼4000 G) could produce the observed emission by synchrotron radiation during the 2003 November 2 burst. Positrons created by π± decay during nuclear reactions have a very broadband emission peaks in the far infrared (Lingenfelter & Ramaty 1967), and so are good candidates for explaining the submillimeter increase. da Silva et al. (2007) have searched for evidence of positrons to originate the 2003 November 2 submillimeter flux increase without success: the number of positrons needed to produce the observed emission is 5 orders of magnitude more than the one derived from γ and hard X-ray observations. Trottet et al. (2008) arrived at a

similar conclusion when they analyzed the 210 GHz emission of the X17.2 flare of 2003 October 28.

A completely different scenario, which simultaneously explains the increasing submillimeter spectrum and the well-known microwave spectrum, was proposed by Kaufmann & Raulin (2006). The same charged particles that emit synchrotron at submillimeter range undergo microbunching instabilities that produce coherent synchrotron emission at microwave frequencies. Finally, another possible mechanism for explaining the submillimeter increasing spectrum is thermal free-free emission. However, it was argued that the same source should produce a much more intense flux in soft X-rays than the one observed (da Silva et al. 2007).

In this work we present a burst with two spectral components: the classical microwave spectrum with its *inverted V* shape centered near 10 GHz and a high-frequency component with a peak at around 200 GHz, which occurred during an M6.8 class flare. Both characteristics are singular to this event, meaning it is the first time that a flare with a class lower than X shows a separated submillimeter component and that this component is not increasing with frequency. The organization of this paper is as follows. In Sect. 2 we present the observations. A detailed analysis of the magnetic topology is presented in Sect. 3. We discuss the origin of the observed radio emission in Sect. 4, while our main conclusions are presented in Sect. 5.

2. Chromospheric and coronal observations

On 20 December 2002 at around 13:15 UT, an M6.8 class flare occurred in active region (AR) 10226. A radio burst observed by many radio telescopes around the world is associated with this event. At 1.415, 2.695, 4.995, 8.800, and 15.400 GHz frequencies, the USAF Radio Solar Telescope Network (RSTN) provides solar patrol data with 1 s time resolution. We also have observations at 8.4, 11.8, 19.6, 35, and 50 GHz from the Bern Patrol telescopes, while at 89.4 GHz the two-element nulling interferometer of the University of Bern provides total flux measurements with a sensitivity of ~35 s.f.u. (1 s.f.u. = 10^{-22} W m^{-2} Hz^{-1}) and a time resolution of 31 ms (Lüthi et al. 2004a).

At frequencies higher than 200 GHz we have data from the SST (Kaufmann et al. 2001). This is a multibeam system with 4 beams at 212 GHz and 2 beams at 405 GHz in the focus of the antenna. The telescope is enclosed in a Gore-Tex radome, the radiometers are at room temperature, the antenna is pointed with an Orbit positioner, and the whole system is controlled by a PC running its own controlling and acquisition software. The sensitivity of the instrument is better than 1 s.f.u., and the time resolution is 5 ms. At 212 GHz the system can determine the centroid position of the emitting source because three beams overlap at the 50% level of its HPBW (see Giménez de Castro et al. 1999, and references therein). The absolute uncertainty in position is around 30″, but relative displacements have uncertainties on the order of 1″. The observations are calibrated against two thermal sources, assuming that the detectors have a linear response. We also get rid of the sky attenuation by assuming a plane parallel atmosphere and correcting the absorption. The zenith opacity is measured two or three times per day. The data are converted to temperature, corrected by sky absorption, and the absolute flux density determined with the multibeam system. Overall, a 40% uncertainty in flux density can be considered.

Figure 1 shows the time evolution of the flux density at selected frequencies. In radio the flare is characterized by two separate events, with the first one starting at around 13:15 UT and
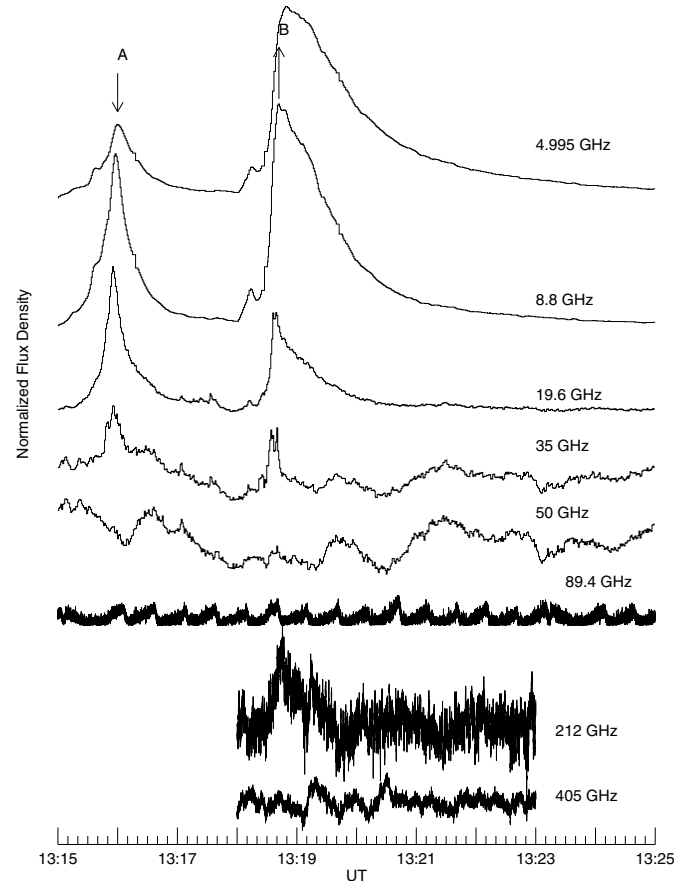

Fig. 1. Normalized flux density time evolution at selected frequencies. The labels A and B mark the time at which the radio spectra are shown in Fig. 3.

lasting 2 min. The second event starts at 13:18 UT with a similar duration. At submillimeter frequencies, only the second burst was recorded because the antenna was performing calibration routines before. The burst is observed from metric waves up to 35 GHz. At 50 and 89.4 GHz, the noise dominates the emission and only an upper bound limit can be determined. Surprisingly, at 212 GHz the emission of the second burst is stronger than the noise, but at 405 GHz the signal is dominated by the noise again. It is also interesting to compare the radio time evolution with the soft X-ray emission. Figure 2 shows the flux in the 1–8 Å band from the GOES 10 satellite with the emission at 15.4 GHz.

The radio spectrum at instant A is shown in the top panel of Fig. 3. The turnover frequency is around 10 GHz. The uncertainty in flux density was considered 10% for all frequencies, except at 35 GHz because the changes of its base line (mainly sky emission) were taken into account. In this case we consider an uncertainty of 40%. At 50 and 89.4 GHz, we can only refer to an upper bound limit. On the low-frequency range of the spectrum, where the emission is optically thick, the flux density at 4.995 and 2.695 GHz is higher than expected for a purely homogeneous gyrosynchrotron emission. Furthermore, spectrograms reveal an intense metric/decimetric emission (see, e.g. Phoenix-2 results at http://www.astro.phys.ethz.ch/rapp/rapp_home_nf.html). Therefore, the excess flux observed below 5 GHz can be attributed to coherent emission.

The spectrum at instant B is not very different, because the maximum flux and the turn over frequency are almost the same as during A. The main characteristic is the appearance of emission at 212 GHz, which is more intense than the maximum upper
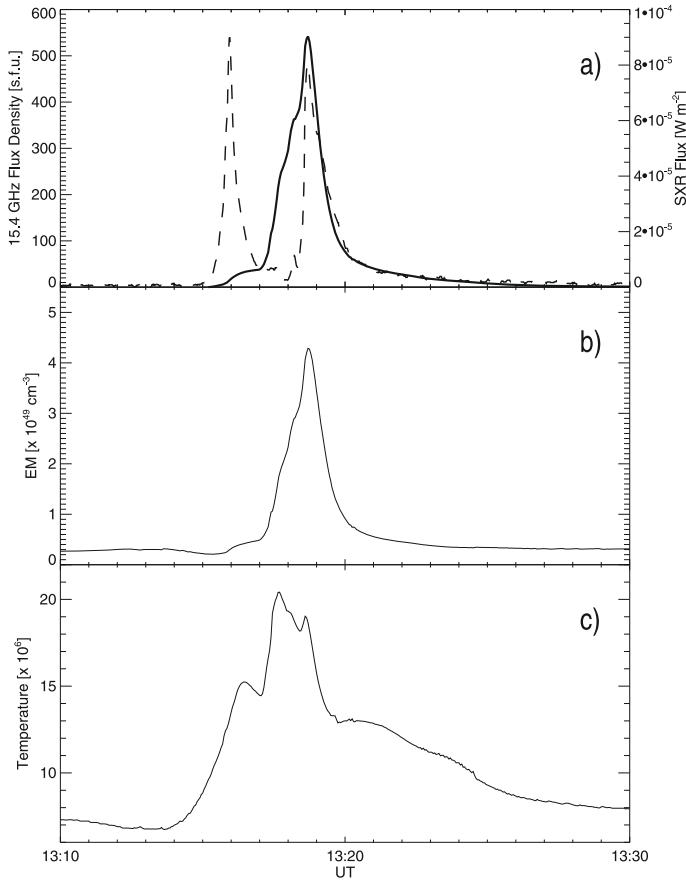
Fig. 2. a) GOES 1–8 Å flux (continuous curve) with 15.4 GHz flux density (dashed curve). **b)** Emission measure (EM). **c)** Temperature.

bounds at 89.4 and 405 GHz. We want to point out that, at 89.4 and 405 GHz, we only have upper limits and cannot see a time evolution of the emission in the same way as at 212 GHz (Fig. 1).

Figure 4 shows an EUV 195 Å image taken by the Extreme Ultraviolet Imaging Telescope (EIT, Delaboudinière et al. 1995) aboard the SoHO satellite at 13:19:38 UT, the closest image to flare maximum. The circles represent the SST beams: 2, 3, and 4 correspond to the 212 GHz multibeam system, while 5 is the 405 GHz beam. Beam 1 (212 GHz) is beyond this image and beam 6 (405 GHz) was not working on that day. The centroid position is the gray area inside beam 5. As stated, our absolute uncertainty is around 30″; therefore, the solutions are compatible with the EUV bright kernels inside beam 2.

The Hα images show three bright kernels (Fig. 5) that brighten with different timing (Fig. 6). Kernel 1 is better correlated with the first burst (Fig. 6b), while kernel 3 is correlated with the second burst (Fig. 6d), although a flux increase is also seen during the first burst. The flux of kernel 2 seems to increase between the two bursts and is the most intense. Unfortunately, we have no data at 212 GHz during the first burst to analyze the time evolution of the centroid positions.

3. Photospheric observations and modeling

3.1. The magnetic-field evolution

To study the evolution of the AR magnetic field, we used full-disk level 1.5 magnetograms obtained by the Michelson Doppler Imager (MDI, Scherrer et al. 1995) aboard SoHO. These data are the average of 5 magnetograms with a cadence of 30 s. They are
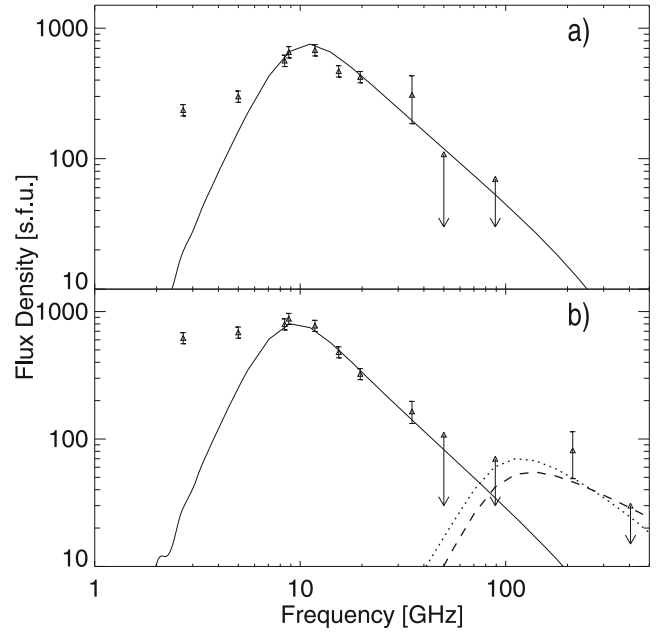

Fig. 3. a) Radio spectra at instant A; **b)** Radio spectra at instant B (see Fig. 1). The curves represent the obtained gyrosynchrotron solutions (see text).
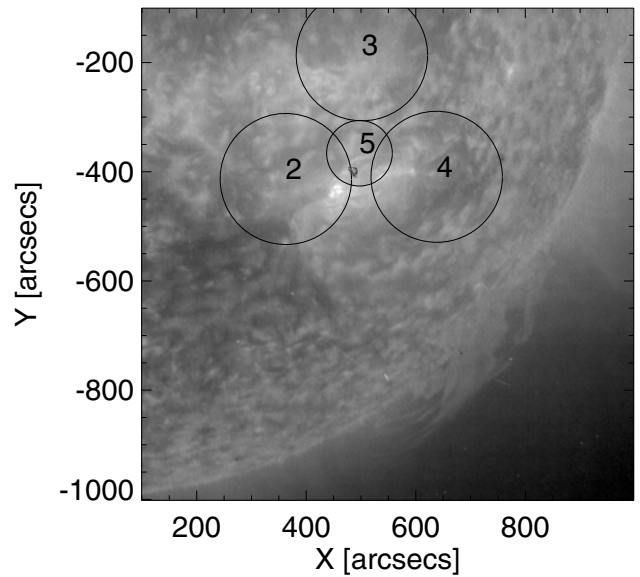

Fig. 4. An EUV 195 Å image taken by the EIT telescope aboard the SoHO satellite at 13:19:38 UT. Superimposed on the image, the circles represent the SST beams at the moment of the burst. Beams 2, 3, and 4 (212 GHz) are the multibeam system. Beam 5 is the 405 GHz receiver. The centroid position obtained with the SST is the gray area inside beam 5. North is up and west is to the right in this and subsequent images.

constructed once every 96 min. The error in the flux densities per pixel in the averaged magnetograms is ≈9 G, and each pixel has a mean area of 1.96 Mm^2. We produced a magnetic field movie starting at the time of the AR appearance and extending for nine days.

AR 10226 was seen on the solar southern hemisphere on 13 December 2002. The AR was originally bipolar and followed the Hale-Nicholson law for solar cycle 23rd (Hale & Nicholson 1925). The main polarities (bipole A) grew in size and intensity and separated from each other, as happens during emergence of a
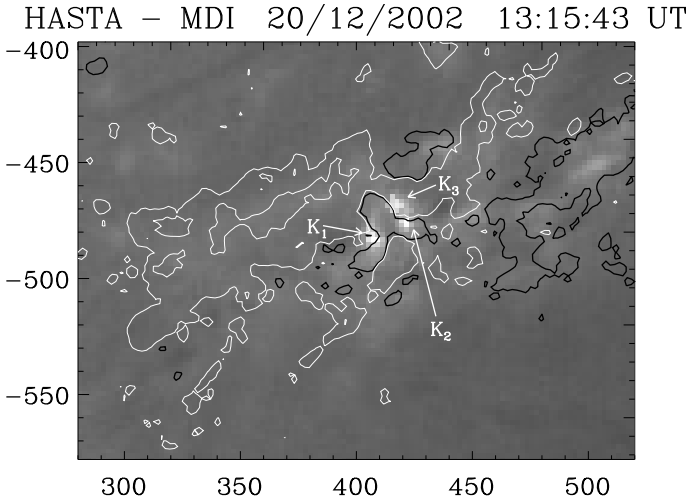
Fig. 5. An Hα image at 13:15:43 UT showing the three kernels. MDI contours of ±100 G have been added (withe/black colour corresponds to positive/negative values).

flux tube having the typical shape of the letter Ω (see e.g. Zwaan 1987, and references therein). During the initial emergence period, the preceding negative polarity elongated below the following one (see Fig. 7a), as expected because of the azimuthal component of the field contributing to the vertical component during emergence of a flux tube with a positive magnetic twist (López Fuentes et al. 2000).

By 15 December an oppositely oriented bipole (bipole B), forming a quadrupolar configuration with the main AR polarities, started emerging, and was clearly visible by 17 December (see Fig. 7b). As this bipole evolved, the two polarities rotated around each other and separated in such a way that the positive polarity moved above the negative one (see Fig. 7c); finally, both polarities reached the original AR bipole orientation. The behavior just described is the one expected during the emergence of a kinked deformed flux tube having a positive writhing of its axis (Linton et al. 1998, 1999; Fan et al. 1999). Several examples of bipoles showing such an evolution have been analyzed by Mandrini et al. (2002) and López Fuentes et al. (2003).

In the early morning of 20 December another emergence, as the one described, occurred in its close vicinity. Again, a small bipole (bipole C) was observed appearing with a reversed orientation and rotated to the original AR bipole orientation (see Fig. 7d). The Hα and EUV kernels of the flare analyzed in this work are associated with these two emergences. It is in this zone of the AR where most of the flare activity was concentrated during the region disk transit (see http://sgd.ngdc.noaa.gov/sgd/jsp/solarindex.jsp). Minor magnetic-field emergence, starting approximately two days after the AR appeared on the disk, occurred during the whole AR transit along the main AR inversion line as can be seen in Figs. 7.

The evolution of the AR field is consistent with the emergence of a twisted flux tube across the photospheric surface. Schuessler (1979), as well as Longcope et al. (1996), showed that non-twisted buoyant flux cannot even surface, since untwisted flux tubes tend to fragment as they rise through the convection zone. Both 2D (Moreno-Insertis & Emonet 1996; Emonet & Moreno-Insertis 1998) and 3D models (Abbett et al. 2000; Fan 2001) predict that flux tubes with a certain amount of twist would survive the interaction with the surrounding plasma as they travel through the convective zone. On the other hand, as the flux tube rises through the convective zone, turbulent rolls
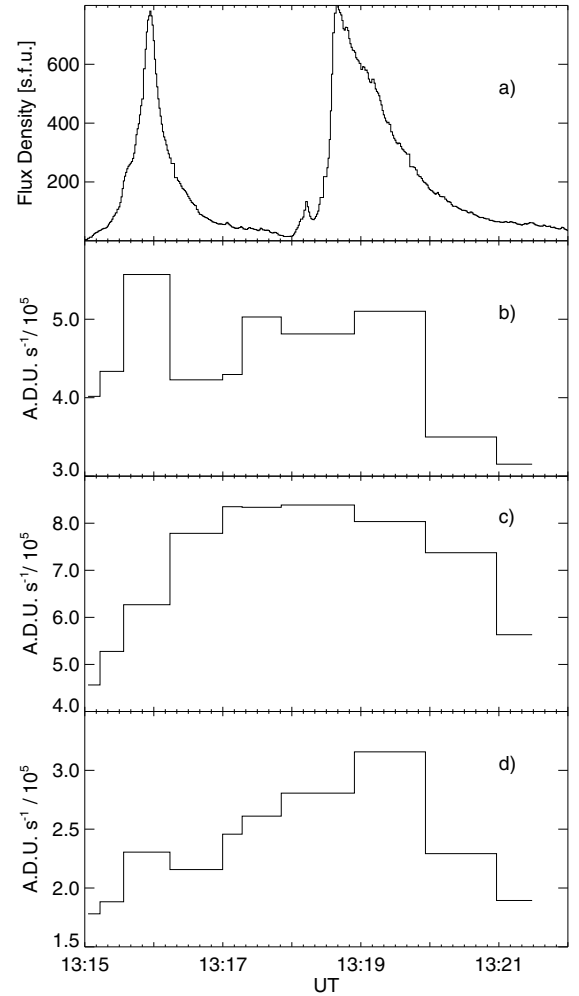

Fig. 6. Hα flux time evolution. **a)** 11.8 GHz time profile, **b)** Hα flux of kernel 1, **c)** Hα flux of kernel 2, and **d)** Hα flux of kernel 3 (see Fig. 5 for a description of the kernels).

develop in the back part of the tube (as when a rigid body moves in a fluid) (see e.g. Emonet & Moreno-Insertis 1998). The magnetic field in this region is then shredded into smaller portions that, due to a lower magnetic pressure, will probably surface later than the top part of the original buoyant tube. These smaller portions would then be seen as secondary emerging bipoles on the photospheric surface in the vicinity of the main AR bipole. If one of these portions has a twist at the level of being kinked, its photospheric crossing would appear like the one of bipole B.

3.2. Magnetic field modeling and location of flare kernels

To find clues to the magnetic environment in which the observed flare took place, we extrapolated the photospheric magnetic data to the corona. The coronal field is computed under the linear (constant α) force-free field assumption ($\nabla \times \boldsymbol{B} = \alpha\boldsymbol{B}$), using a fast Fourier transform method, as proposed by Alissandrakis (1981). Our model takes into account the transformation of coordinates from the AR location to disk center (see e.g. Mandrini et al. 1996; Démoulin et al. 1997).

The top image in Fig. 8 shows a set of coronal loops observed by EIT before the event analyzed here, on 20 December at 12:48 UT; while the figure below is a model of the coronal magnetic field. As boundary condition for the model, take the MDI magnetogram closest in time to the flare (Fig. 7d). The
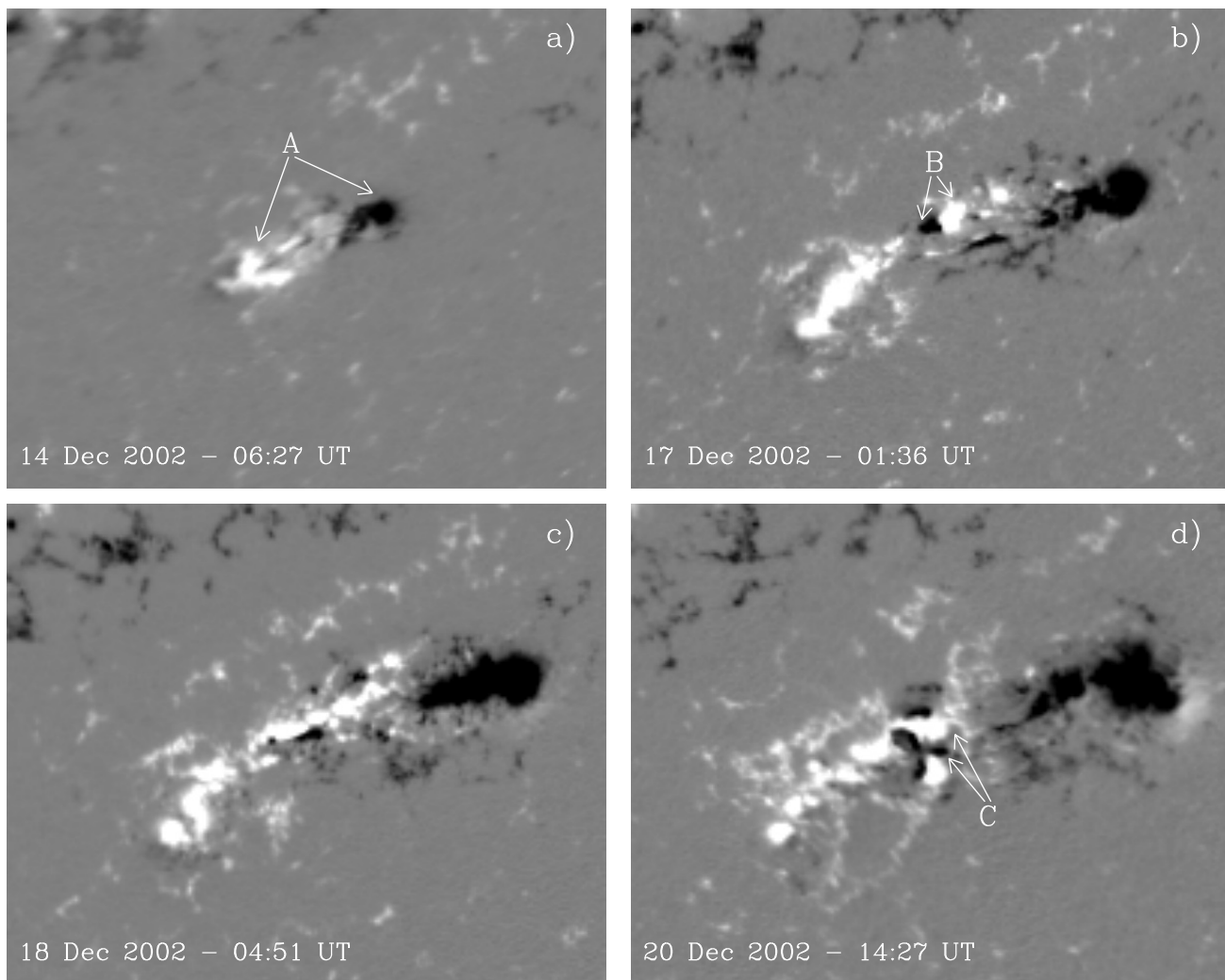
Fig. 7. Photospheric magnetic field evolution. **a)**, **b)**, **c)**, and **d)** show the line-of-sight magnetic field of AR 10226 from 14 December to 20 December. The images cover an area of 170 pixels × 136 pixels (1 pixel side ≈1.96″). The letters correspond to the bipoles described in the text, and arrows point to the positive and negative polarities of these bipoles. The data represented on a gray scale are saturated above (below) 500 G (−500 G).

value of the free parameter α is determined to best fit the EIT loops observed in 195 Å in the image above. No coronal loops could be distinguished during the flare; then, to determine the value of α, we took the closest EIT image where loops at different spatial scales appear. However, the flare kernels, which agree with kernels 1, 2, and 3 in Hα (see Fig. 5), are clearly visible in 195 Å during the event.

The value of α is computed through an iterative process. First, we compute the coronal field assuming a given value for α; then, we compute the mean distance between the observed EIT loops and the closest computed field lines. Finally, through successive steps we select the value of α that gives the best global fit (i.e. lowest mean distance), as discussed in Green et al. (2002). We found that three different values of α are needed to match the EIT observed loops best. The largest ($\alpha = 1.51 \times 10^{-2}$ Mm^{-1}) gives better agreement to the loops at the north of the AR, while the intermediate and lowest ($\alpha = 0.75 \times 10^{-2}$ Mm^{-1} and $\alpha = 0.31 \times 10^{-2}$ Mm^{-1}, respectively) fit the loops rooted at the south of the AR better (with α decreasing as the height of the loops increases, see Schmieder et al. 1996). In all cases, α is positive as suggested by the shape of the photospheric polarities during emergence (see Sect. 3.1).

Taking into account the magnetic field evolution described in Sect. 3.1 and the location of flare kernels, the analyzed event could have been initiated by the interaction of bipole C with the pre-existing bipole B (see Figs. 5 and 7). Therefore, we analyze the magnetic connectivity between these bipoles in the neighborhood of the flare kernels. Figures 9a and b show a set of thin continuous field lines linking the polarities belonging to both bipoles B and C. These field lines are rooted in the vicinity of the flare kernels. See the next paragraph for a discussion on the value of α in Fig. 9. The interaction, via magnetic reconnection, between these bipoles could have given place to the two microwave bursts that occurred during the studied flare, as discussed in Sect. 5.

The energy released by magnetic reconnection between bipoles B and C is then deposited at chromospheric level giving place to the observed flare kernels in Hα and also in 195 Å (see Figs. 4 and 5). The kernel to the northwest is located in the positive polarity of bipole C, while the one to its south lies in the negative polarity of the same bipole. On the other hand, the third kernel to the east elongates between the positive and negative polarities of bipole B, and the shape of this kernel follows the magnetic inversion line at that location. We have found that to connect the flare kernels (or the region in their vicinity)
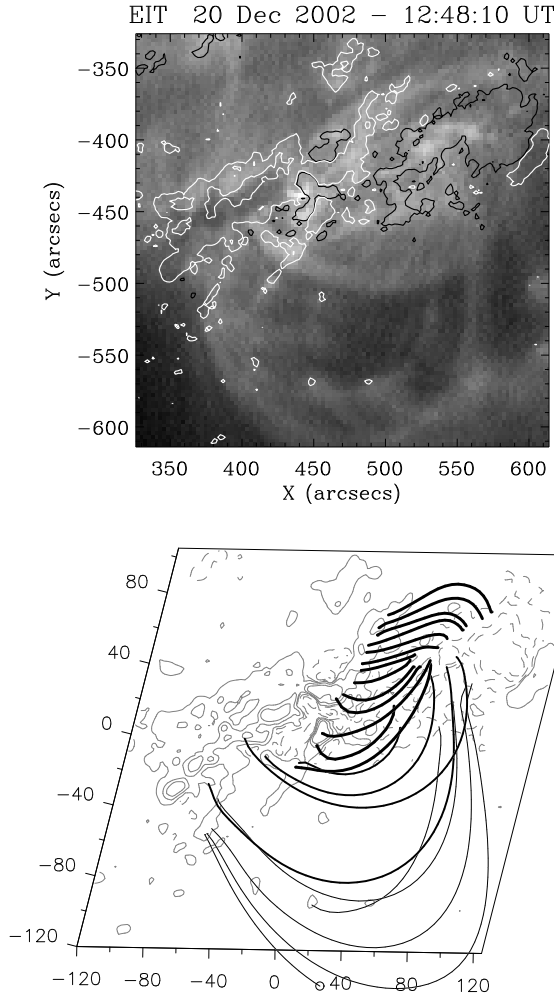
Fig. 8. EIT 195 Å observations and magnetic field model. The *top panel* shows an EIT image at 12:48 UT. Some EIT loops are clearly seen at this time. MDI contours of ±100 G have been added (white/black continuous line corresponds to the positive/negative value). Both axes are measured in arcsec. The *bottom panel* corresponds to an MDI image at 14:27 UT showing the same field of view as the top one. Positive/negative isocontours (±100, 500, 1000 G) are drawn with gray continuous/dashed thin lines. The absolute contour values progressively increase from the outer to the inner ones. Some magnetic field lines following the shape of EIT loops have been superimposed (the values of α from the thickest to the thinnest field lines are 1.51×10^{-2} Mm^{-1}, 0.75×10^{-2} Mm^{-1} and 0.31×10^{-2} Mm^{-1}, respectively). Both axes are measured in Mm.

with field lines rooted in bipoles B and C, we need to increase the value of α as much as 6.03×10^{-2} Mm^{-1}. This is consistent with the fact that the flux tube forming bipole B could have been twisted enough to be kinked. The set of thick continuous field lines in Fig. 9 would be the result of the interaction between bipoles B and C, these lines have footpoints in the positive polarity of bipole C and the negative of bipole B. The other set of reconnected field lines should be rooted in the positive polarity of bipole B and the negative of bipole C; however, we have not been able to compute lines for this set even with the highest α value. It is possible that the field is strongly sheared locally and then a linear force-free model, like the one we are using, cannot represent the real magnetic configuration; unfortunately, there are no vector magnetic field observations available to confirm this assumption. Figure 9b shows the connectivity before and after magnetic reconnection from a different perspective. In
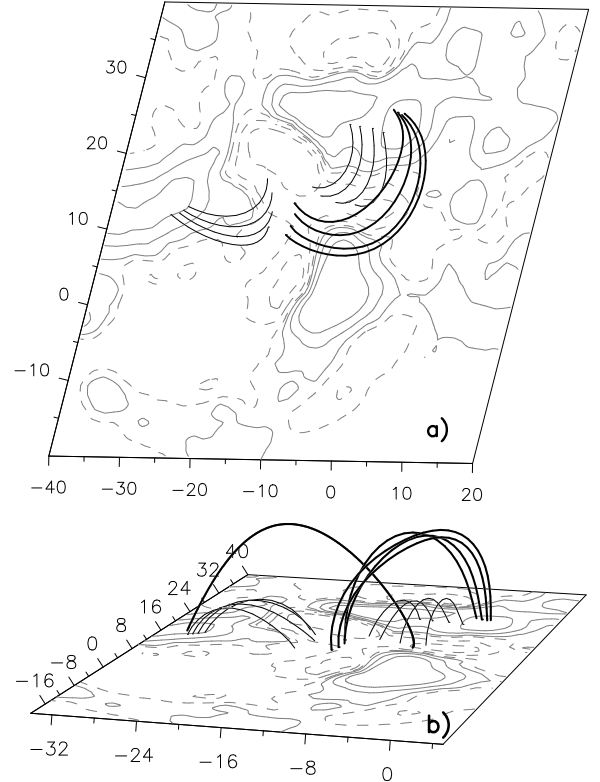

Fig. 9. Magnetic field model showing the field line connectivity in the vicinity of flare kernels. Panel **a)** corresponds to the observer's point of view. We computed magnetic field lines anchored in both polarities of bipoles B and C. Thin continuous field lines represent the connectivities before magnetic reconnection has occurred, while thick continuous field lines are the ones after reconnection. Only one set of reconnected lines can be computed using a value of $\alpha = 6.03 \times 10^{-2}$ Mm^{-1}. The other set is represented by one line added to panel **b)**, this figure has been drawn from a different perspective. The isocontours of the field are ±100, 500, 1000 G, using the same convention as in Fig. 8. The absolute contour values progressively increase from the outer to the inner ones. All axes are measured in Mm.

this figure we have drawn a single thick continuous line to represent the second set of reconnected field lines.

4. Physical parameters derived from observations

4.1. Physical environment of the emitting region

We first concentrate on the determination of the physical characteristics of the region producing the soft X-ray emission. As shown in the preceding section, AR 10226 showed many changes in its magnetic field structure and topology during its disk transit, including several episodes of the emergence of twisted and kinked flux tubes in its central portion. It is in this region that the flaring activity studied in this paper was concentrated, as shown by HASTA images and corroborated by EIT observations obtained after the impulsive burst at interval B. The Hα observations show that, during interval A, the activity mostly concentrated towards the east (at these early times kernel 1 clearly shows the burst signature), while the second burst at B is more noticeable in kernel 3.

Although no hard or soft X-ray images are available to study this event, the evolution of the flux measured by GOES (Fig. 2), as well as of the temperature and emission measure of the soft

X-ray emitting plasma, give us some clues regarding the multiple loop structure of the event and the relative contribution of the different bipoles. Looking first at the temperature time evolution, we note that it shows an early rise and a first peak at 13:16:20 UT, clearly associated with the energy release during interval A , which is followed by a slow emission measure rise. This early peak is followed by a second one, some 120 s later, that reaches a temperature of $\sim 2 \times 10^7$ K, the maximum obtained from GOES records during the event. The most remarkable feature associated with this maximum, which corresponds to interval B, is the extremely rapid rise and fall of the soft X-ray flux (Fig. 2), which is reflected in the emission measure timeline that reaches a maximum of 4.3×10^{49} cm^{-3} at 13:18:43 UT. This coincides with the appearance of the 212 GHz burst component and with a clear peak in the Hα lightcurve of kernel 3. Offhand, the temporal behavior of the X-ray emission is indicative of a compact and dense region, something that is supported by how it seems to originate in the small intermediate region of flux emergence (bipoles B and C). The compactness of the region is corroborated by the separation of the Hα kernels, which is less than 20″ between kernels 1 and 2 and about 10″ between kernels 2 and 3.

More quantitative estimates can be obtained using the characteristic decay times, τ, of the X-ray plasma temperature and emission measure that we may equate to either the conductive and radiative cooling timescales (Tandberg-Hanssen & Emslie 1988), to obtain plausible estimates of the physical parameters of the emitting region. These times range from 50 to 123 s but, for the sake of simplicity and considering that the values are derived from the spatially unresolved GOES data, we take $\tau \sim 100$ s. Equating this value to the radiative cooling timescale τ_r,

$$\tau_r = \frac{3nk_B T}{n^2 \Phi(T)} = \frac{3k_B T}{n\Phi(T)}, \tag{1}$$

where $\Phi(T)$ is the radiative loss function (Raymond et al. 1976), n and T are the plasma density and temperature respectively, and k_B is the Boltzmann constant, we obtain $n \sim 3.4 \times 10^{12}$ cm^{-3}. Doing the same with the conductive timescale τ_c, given by,

$$\tau_c = \frac{3nk_B T L^2}{1.1 \times 10^{-6} T^{7/2}}, \tag{2}$$

where L is the characteristic loop length, we obtain $nL^2 \sim 5.3 \times 10^{29}$ cm^{-1} from which we derive $L \sim 7.3 \times 10^8$ cm if $n \sim 10^{12}$ cm^{-3}; or if we assume $L = 10^9$ cm, we get $n \sim 5.3 \times 10^{11}$ cm^{-3}.

A further estimate can be obtained using the rise timescale of the emission measure, assuming that it represents the filling-in of the flaring loop(s) through chromospheric evaporation. The value of the rise timescale ranges between 65 and 90 s. If we equate these values to the hydrodynamic timescale τ_h, given by,

$$\tau_h = \frac{L}{\sqrt{k_B T / m_p}}, \tag{3}$$

where m_p is the proton mass, we find $1.9 \times 10^9 \leq L \leq 2.6 \times 10^9$ cm.

From all these estimates and keeping in mind that the emission measure was close to its maximum (4×10^{49} cm^{-3}) at the time of the 212 GHz peak, we can obtain a range for the estimated mean cross-section A of the flaring loop or loops. Thus, from the values quoted above, we find 6×10^{16} cm^2 $\leq A \leq 1.5 \times 10^{17}$ cm^2, which can be compared with the area of kernel 3, which is $A_{k_3} = 1.8 \times 10^{17}$ cm^2 estimated from Hα observations. We chose kernel 3 because it is the one that shows the most clear temporal correspondence with the 212 GHz emission (for comparison, the areas of the other Hα kernels are $A_{k_2} = 2.9 \times 10^{17}$ cm^2 and $A_{k_1} = 4.7 \times 10^{17}$ cm^2). From A_{k_3} and a loop length on the order of 10^9 cm, we once again obtain an average density of $n \sim 10^{12}$ cm^{-3}.

In both cooling timescale analysis (no matter the actual cooling mechanism), as well as in the case when we consider the hydrodynamic timescale related to chromospheric evaporation, we are led to a similar set of parameters that imply a compact source of high density. Summarizing, the physical parameters prevailing in the region where the submillimeter burst component originated, imply source sizes similar to those derived using a different technique by Lüthi et al. (2004b). The region is a rather compact ($L \sim 10^9$ cm) and dense ($n \sim 10^{12}$ cm^{-3}) loop or loop system, rooted in a high magnetic-field region. The significance of these results is discussed in the next section.

4.2. Origin of the radio emission

The radio emission at low frequencies is gyrosynchrotron radiation from accelerated electrons. We can use Ramaty (1969) derivations to compute the expected emission of a homogeneous source having as a constraint the magnetic topology derived in Sect. 3. We know that the magnetic field should be on the order of hundreds of Gauss and the source size should not be more than a few tens of arc seconds. With this in mind, we are able to fit a solution to the spectrum at interval A (Fig. 3, top panel), which yields a total number of 10^{35} electrons with a power-law index $\delta = 3.2$ and a cutoff energy $E_\circ = 25$ keV, embedded in a 200 G magnetic field. The source has a diameter of 9″and its height is 5×10^8 cm. The optically thick part of the spectrum below 5 GHz cannot be adjusted by this solution probably because the coherent emission is more intense. Furthermore, if the gyrosynchrotron emission originates at the same place where the soft X-rays are emitted, i.e. a region with $n \sim 10^{12}$ cm^{-3}, frequencies below 9 GHz would be totally absorbed. The source size and the number of electrons in the beam agree with the results derived from soft X-ray observations in the previous section.

The search for a solution during interval B gives similar results for the low frequencies (Fig. 3, lower panel). However, as expected, the flux at 212 GHz cannot be fitted with this solution. A thermal free-free source can be discarded because the upper limit of the emission at 405 GHz is significantly less than the intensity observed at 212 GHz. Therefore, the submillimeter emission can only be synchrotron. Since the number of points of the spectrum to fit is reduced to one (212 GHz) and two constraints (at 89.4 and 405 GHz), it is not possible to find a unique solution using Ramaty's code. Nonetheless, we can give an order of magnitude estimate for the parameters. A strong magnetic field is needed to have the turnover near 200 GHz. We consider a view angle of 70°, which restricts the magnetic field to a minimum value and is coherent with the position of the AR near the west limb. For this minimum magnetic-field value, we take 2000 G, which is consistent with MDI observations at the location of kernel 3. We also consider an electron index lower than for the low-frequency range, $\delta_H = 2.1$, and an energy cutoff $E_\circ = 25$ keV. For the source we take a cylinder of 0.17″ diameter and 10^8 cm height, a value that is justified by the scenario proposed in Sect. 5. A plasma density $n = 9 \times 10^{11}$ cm^{-3} is used in the calculations. Consequently, the total number of electrons is not very high $\sim 5 \times 10^{30}$. The dashed curve in Fig. 3b shows this solution, which is compatible with the spectrum.

A weaker magnetic field could be considered if the auto-absorption of the accelerated electrons increases, i.e. if the

electron beam density increases. For instance for a 500 G magnetic field, we need a beam electron density $n_e \sim 10^{11}$ cm^{-3}. Since, according to the previous section, the plasma density is close to $n \sim 10^{12}$ cm^{-3}, this would mean that the accelerator mechanism should have had a very high efficiency to achieve the required n_e.

5. Discussion and conclusions

We present a multiwavelength analysis of a solar event with an spectral component observed only in the submillimeter range. Unlike previous examples (Kaufmann et al. 2004, 2007; Lüthi et al. 2004b; da Silva et al. 2007), the submillimeter component is only observed at 212 GHz and it occurred during a flare of class lower than X.

Observations in different wavelengths (Hα, radio, EUV, and soft X-rays), combined with the study of the magnetic field evolution and modeling, lead us to the following flare scenario. As bipole C emerges in the pre-existing magnetic environment of bipole B, magnetic reconnection occurring in the low chromosphere can accelerate electrons that will produce the observed microwave emission as they spiral along the magnetic field lines. This first energy-release process, which would correspond to the first radio burst, will also produce emission at the chromospheric level. Concerning the EUV emission, EIT time resolution (1 image every 12 min) does not allow us to distinguish both flare bursts. Energy release could proceed continuously, but if part of the overlaying magnetic field is removed by reconnection, a certain time (while bipole C continues emerging) would be required to build up a current layer thin enough for reconnection to be efficient (see the simulations by Aulanier et al. 2006). Then, a second burst can happen, the one when we observe radio emission at frequencies above 100 GHz. An asymmetry present in the reconnected loops could explain the almost simultaneous presence of both low and high frequency emission. If one of the footpoints of the reconnected lines is anchored in a region of higher magnetic field than the other one, we expect that electrons accelerated towards this footpoint would be mirrored towards the other one (see e.g. the set of thick continuous field lines in Figs. 9). These electrons would produce low-frequency emission by gyrosynchrotron along the upper coronal portion of the loop or loops and high-frequency emission as they travel in regions with a higher magnetic field to which they have access. This would imply that, from the two models proposed to explain the radio emission above 100 GHz, the one requiring a magnetic field of 2000 G is the most plausible one. We note that this magnetic field strength is only a lower limit, although the other physical magnitudes have reasonable values. Only a very small portion ($\sim 10^{-5}$) of the accelerated electrons is mirrored, and in this process, its distribution hardens as can be deduced by the increase in the electron index, from $\delta = 3.2$ (microwave index) to $\delta_H = 2.1$ (submillimeter index). Nonetheless, we stress that this later value was chosen to obtain a lower limit for the magnetic field strength, since we do not observe the optically thin part of the submillimeter spectrum. The proposed scenario is then compatible with all the physical parameters deduced from observations in Sect. 4. Furthermore, since the magnetic field evolution and topology that give rise to both radio bursts is basically the same (emergence and reconnection between bipoles B and C), we expect that, if we had observed emission at frequencies above 100 GHz during the first burst, we would have found a similar spectrum to the one observed during the second burst.

Moreover, the emission at frequencies above 100 GHz cannot be synchrotron of positrons produced during nuclear reactions because its expected spectrum is very wide and peaks in the far infrared (e.g. Lingenfelter & Ramaty 1967). Thermal bremsstrahlung (free-free) can also be discarded because its spectrum is expected to be wider than the one observed in this flare.

As a final note, we observe that homogeneous models cannot account for the radio emission along the whole spectrum and that the topological analysis of the magnetic field gives keys to how the emission is produced.

References

Abbett, W. P., Fisher, G. H., & Fan, Y. 2000, ApJ, 540, 548
Alissandrakis, C. E. 1981, A&A, 100, 197
Aulanier, G., Pariat, E., Démoulin, P., & Devore, C. R. 2006, Sol. Phys., 238, 347
da Silva, A., Share, G., Murphy, R., et al. 2007, Sol. Phys., in press
Delaboudinière, J.-P., Artzner, G. E., Brunaud, J., et al. 1995, Sol. Phys., 162, 291
Démoulin, P., Bagala, L. G., Mandrini, C. H., Henoux, J. C., & Rovira, M. G. 1997, A&A, 325, 305
Emonet, T., & Moreno-Insertis, F. 1998, ApJ, 492, 804
Fan, Y. 2001, ApJ, 546, 509
Fan, Y., Zweibel, E. G., Linton, M. G., & Fisher, G. H. 1999, ApJ, 521, 460
Giménez de Castro, C. G., Raulin, J. P., Makhmutov, V. S., Kaufmann, P., & Costa, J. E. R. 1999, A&AS, 140, 373
Green, L. M., López fuentes, M. C., Mandrini, C. H., et al. 2002, Sol. Phys., 208, 43
Hale, G. E., & Nicholson, S. B. 1925, ApJ, 62, 270
Kaufmann, P., & Raulin, J.-P. 2006, Phys. Plasmas, 13, 701
Kaufmann, P., Costa, J. E. R., Giménez de Castro, C. G., et al. 2001, in Proc. of the SBMO/IEEE MTT-S International Microwave and Optoelectronics Conference, 439
Kaufmann, P., Raulin, J. P., de Castro, C. G. G., et al. 2004, ApJ, 603, L121
Kaufmann, P., Trottet, G., Giménez de Castro, C., et al. 2007, in American Astronomical Society Meeting Abstracts, 210, 93
Lingenfelter, R. E., & Ramaty, R. 1967, Planet. Space Sci., 15, 1303
Linton, M. G., Dahlburg, R. B., Fisher, G. H., & Longcope, D. W. 1998, ApJ, 507, 404
Linton, M. G., Fisher, G. H., Dahlburg, R. B., & Fan, Y. 1999, ApJ, 522, 1190
Longcope, D. W., Fisher, G. H., & Arendt, S. 1996, ApJ, 464, 999
López Fuentes, M. C., Demoulin, P., Mandrini, C. H., & van Driel-Gesztelyi, L. 2000, ApJ, 544, 540
López Fuentes, M. C., Démoulin, P., Mandrini, C. H., Pevtsov, A. A., & van Driel-Gesztelyi, L. 2003, A&A, 397, 305
Lüthi, T., Lüdi, A., & Magun, A. 2004a, A&A, 420, 361
Lüthi, T., Magun, A., & Miller, M. 2004b, A&A, 415, 1123
Mandrini, C. H., Demoulin, P., van Driel-Gesztelyi, L., et al. 1996, Sol. Phys., 168, 115
Mandrini, C. H., López Fuentes, M. C., Démoulin, P., van Driel-Gesztelyi, L., & Pevtsov, A. A. 2002, in SOLMAG. Proceedings of the Magnetic Coupling of the Solar Atmosphere Euroconference, ed. H. Sawaya-Lacoste, ESA SP, 505, 121
Moreno-Insertis, F., & Emonet, T. 1996, ApJ, 472, L53
Ramaty, R. 1969, ApJ, 158, 753
Raymond, J. C., Cox, D. P., & Smith, B. W. 1976, ApJ, 204, 290
Scherrer, P. H., Bogart, R. S., Bush, R. I., et al. 1995, Sol. Phys., 162, 129
Schmieder, B., Demoulin, P., Aulanier, G., & Golub, L. 1996, ApJ, 467, 881
Schuessler, M. 1979, A&A, 71, 79
Tandberg-Hanssen, E., & Emslie, A. 1988, The Physics of Solar Flares (Cambridge, GB: Cambridge University Press)
Trottet, G., Krucker, S., Lüthi, T., & Magun, A. 2008, ApJ, 678, 509
Zwaan, C. 1987, ARA&A, 25, 83